Nano Research

Open Access

Research Article

Steering oxidation pathways via Au-mediated transition from type-II to Z-scheme for high-efficiency NO deep oxidation with near-zero NO_2 emission

Xingyan Liu[1,§], Kaili Wu[1,§], Yue Li[1], Youzhou He[1], Yuyu Fang[2] ✉, Min Fu[1], Ben Lei[3] ✉, and Yuhan Li[1] ✉

[1] *Chongqing Key Laboratory of Environmental Catalysis, College of Environment and Resources, Institute for Frontier Interdisciplinary Research in Intelligence and Environment, School of Big Data, Chongqing Technology and Business University, Chongqing 400067, China*
[2] *School of Pharmacy, Chinese Medicine Germplasm Resources Innovation and Effective Uses Key Laboratory of Sichuan Province, Chengdu University of Traditional Chinese Medicine, Chengdu 611137, China*
[3] *School of Materials Science and Engineering, Chongqing Jiaotong University, Chongqing 400074, China*
[§] *Xingyan Liu and Kaili Wu contributed equally to this work.*

Cite this article: *Nano Research*, **2026**, *19*, 94908660. https://doi.org/10.26599/NR.2026.94908660

ABSTRACT: Fundamentally, the type-II and Z-scheme heterojunctions exhibit identical band alignments but diverge in the charge carriers transfer mechanisms. Here, we demonstrate that the Au-mediated heterojunction transition from type-II to Z-scheme dictates the subsequent photocatalytic NO reaction pathway to obtain excellent activity and selectivity. As proven by density functional theory (DFT) calculations, Kelvin probe force microscopy (KPFM), and *in-situ* X-ray photoelectron spectroscopy (XPS), the type-II to Z-scheme heterojunction transition is regulated by incorporating Au nanoparticles as electron bridges within *in-situ* fabricated NH_2-MIL-125/TiO_2 through controllable hydrolysis. This transition maintains robust redox potentials to generate more reactive active species through effectively separated charge carriers under the high-efficient built-in electric field. As a result, the Z-scheme (NH_2-MIL-125/Au/TiO_2) exhibits an impressive NO removal efficiency of 82.0%, surpassing the original NH_2-MIL-125 by 3.7 times and the type-II (NH_2-MIL-125/TiO_2) by 1.2 times, while shows a selectivity of almost 100% toward NO_2^-/NO_3^-. The *in-situ* Fourier transform infrared (FT-IR) and DFT reveal that, in comparison with the type-II favored NO^+ intermediates, the Z-scheme favors NO^- intermediates with enhanced O_2/H_2O activation, enabling ideal Gibbs free energy for NO-to-NO_3^- conversion. This study achieves a metal-nanoparticle-mediated strategy for precisely engineering metal-organic framework (MOF)-based heterojunction architectures, which regulates the NO reaction pathways for efficient environmental purification.

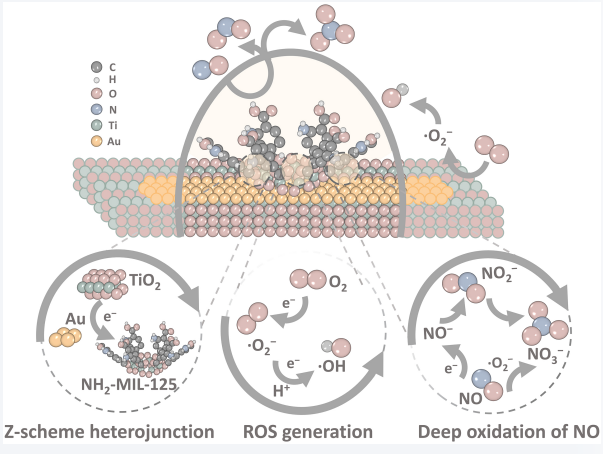

KEYWORDS: MOF-based heterojunction, NO removal, Z-scheme, reactive oxygen species modulation, NO_2 inhibition

1 Introduction

The combustion of fossil fuels releases nitric oxide (NO), which exacerbates environmental pollution such as photochemical smog [1–3]. At ppb levels, NO can persist stably in air for extended periods. Therefore, achieving selective deep oxidation of low-concentration NO while avoiding the formation of the more toxic byproduct NO_2 has become a critical challenge that urgently needs to be addressed in the environmental field. Photocatalysis, which enables the generation of reactive oxygen species under mild conditions to remove pollutants, has emerged as a promising technology for this purpose [4, 5]. The key to photocatalytic NO oxidation lies in controlling the reaction pathway to generate appropriate intermediates [6, 7], thereby facilitating the deep oxidation of NO into the desired final product (nitrate) [8, 9].

The photocatalytic oxidation of NO primarily involves

Received: January 27, 2026; **Revised:** March 11, 2026
Accepted: March 22, 2026

✉Address correspondence to Yuyu Fang, yyfang@cdutcm.edu.cn; Ben Lei, leiben@cqjtu.edu.cn; Yuhan Li, liyh@ctbu.edu.cn

photoinduced electron–hole pair creation and separation, transformation into reactive oxygen species (ROS), and ROS-driven NO oxidation [10, 11]. The effective separation of photoinduced electron–hole pairs critically governs the progression of subsequent steps, while high-yield ROS production facilitates the complete conversion of NO into desirable nitrate products [12]. Although heterojunction construction stands as a prevalent and effective strategy for enhancing charge carrier separation, the conventional type-II heterojunction inevitably compromises redox potentials, thereby diminishing the material's redox capability so as to impede the ROS generation [13, 14]. The insufficient ROS yield usually leads to incomplete NO oxidation, resulting in the formation of toxic byproducts especially the more toxic NO_2 [15]. In contrast, the Z-scheme heterojunction inspired by natural photosynthesis preserves high redox potentials while maintains high-efficient charge carrier separation efficiency through directional electron transport channels [16, 17]. Balancing the relationship between charge carrier separation efficiency and redox capability, along with regulating ROS generation and product selectivity, is crucial for advancing photocatalytic NO removal applications [18, 19].

While type-II and Z-scheme heterojunctions share an analogous band alignment, their charge transfer pathways diverge sharply. [20]. Current researches on heterojunction configuration transformation from type-II to Z-scheme architectures face substantial challenges. Given the intrinsic correlation between Fermi levels and work functions, heterojunction transformation should consider not only band matching but also work function disparities among components, which enables precise control over charge transfer pathways [21]. Notably, the strategic incorporation of noble metal nanoparticles (NPs) (Au, Ag, and Pt) as interfacial electron mediators offers a promising solution by modifying charge redistribution [22]. These metal NPs can optimally function as electronic bridges when sandwiched in intimate contact with both components, which can effectively regulate charge transfer pathways within heterojunction interface, enabling intelligent switch from type-II to Z-scheme configurations [14]. However, the conventional *ex-situ* synthesis approach to metal NPs introduction for heterojunction transformation frequently encounters critical limitations including inadequate interfacial adhesion, lattice mismatches, and suboptimal charge transfer efficiency that restrict effective heterojunction transformation [23, 24].

Metal-organic frameworks (MOFs), distinguished by their exceptional specific surface areas, tunable porous architectures, and abundant coordinatively unsaturated metal sites [25], have emerged as superior templates for engineering *in-situ* heterojunctions with excellent interfacial properties. Among various MOFs, the NH_2-MIL-125 stands out as an ideal candidate for heterojunction engineering due to the synergistic effects between its visible-light-responsive amino-ligands (NH_2-BDC) and catalytically active Ti-oxo clusters [26]. Through pyrolysis or hydrolysis reaction, the partial Ti-oxo nodes within its framework can be controllably transformed into TiO_2, forming a tight NH_2-MIL-125/TiO_2 heterojunction [27, 28]. More importantly, the inherent structure porosity and flexibility of NH_2-MIL-125 facilitate a series of interface engineering. The prior incorporation of Au NPs into NH_2-MIL-125 enables the uniform dispersion of nanoparticles without compromising the structural integrity of the framework, precisely following to controllable hydrolysis to obtain NH_2-MIL-125/Au/TiO_2 with adequate interface effect. By strategically incorporating Au NPs at the interface between NH_2-MIL-125 and TiO_2, they act as electron mediators, reconfiguring the charge transfer pathways and enabling the transformation from a type-II to a Z-scheme configuration. This approach not only addresses the limitation of *ex-situ* constructed heterojunctions but also leverages the unique properties of MOFs to achieve precise control over heterojunction type [29]. Until now, despite the growing interest in heterojunction engineering, current research on MOF-based heterojunctions predominantly focuses on static construction of single types (type-II or Z-scheme), the studies on the transformation heterojunction in MOFs remain scarce.

Building upon above foundation, through Au NPs incorporation, we *in-situ* engineer a solid-state Z-scheme (NH_2-MIL-125/Au/TiO_2, Scheme 1), achieving enhanced NO oxidation performance. Experimental results demonstrate an exceptional NO removal efficiency (82.0%) with stable activity retention over five consecutive cycles and only transient NO_2 detected within initial 5 min (≤ 5 ppb) followed by complete elimination to near 0 ppb. The transition mechanism from the type-II to the Z-scheme heterojunction via Au-mediated bridging layers is in-depth explored by density functional theory (DFT) calculations, *in-situ* Fourier transform infrared (FT-IR), and *in-situ* X-ray photoelectron spectroscopy (XPS). This work establishes a new paradigm for *in-situ* heterojunction fabrication and type regulation in MOFs-based photocatalyst systems for photocatalytic NO deep oxidation.

2 Experimental section

2.1 Synthesis of NH_2-MIL-125

NH_2-MIL-125 was synthesized following a modified literature

Scheme 1 Synthesis of NH_2-MIL-125/Au/TiO_2.

protocol. Briefly, 1.62 g of NH_2-BDC was homogenized in a mixed solvent system containing N,N-dimethylformamide (DMF, 28 mL) and methanol (MeOH, 3 mL). Subsequently, 0.85 mL of titanium butoxide (TBT) was injected dropwise to the homogeneous solution. The resulting mixture was then transferred into Teflon-lined autoclave and subjected to solvothermal treatment (150 °C, 24 h). After cooling to ambient temperature, the precipitate was collected and sequentially washed with DMF and MeOH to remove residual reactants. Finally, the product was vacuum-dried at 60 °C. The specific sources of the experimental reagents can be found in Text S1 of the Electronic Supplementary Material (ESM).

2.2 Synthesis of NH_2-MIL-125/TiO_2

The NH_2-MIL-125/TiO_2 composite was prepared through a hydrothermal deposition process. Initially, 0.4 g NH_2-MIL-125 was ultrasonically suspended in 30 mL of deionized water. This suspension underwent thermal treatment in a flask maintained at 70 °C for 2 h. Following gradual cooling to ambient temperature, the product underwent sequential purification with both water and organic ethanol. The final material was obtained after desiccation under reduced pressure at 60 °C.

2.3 Synthesis of NH_2-MIL-125/Au/TiO_2

The NH_2-MIL-125/Au/TiO_2 composite was prepared through a hydrothermal deposition process. Initially, 0.4 g NH_2-MIL-125/Au was ultrasonically suspended in 30 mL of deionized water. This suspension underwent thermal treatment in a flask maintained at 80 °C for 2 h. Following gradual cooling to ambient temperature, the product underwent sequential purification with both water and organic ethanol. The final material was obtained after desiccation under reduced pressure at 60 °C.

3 Results and discussion

3.1 Characterization

The crystal structures were systematically characterized by X-ray diffraction (XRD) (Fig. 1(a)). The distinct diffraction peaks observed at 6.9°, 9.8°, and 11.9° correspond to the (101), (002), and (211) crystal planes of NH_2-MIL-125, respectively, confirming the successful synthesis of the original NH_2-MIL-125 with high crystallinity [26]. Subsequently, TiO_2 is *in-situ* grown within NH_2-MIL-125 via the hydrolysis reaction of Ti-oxo clusters. The XRD

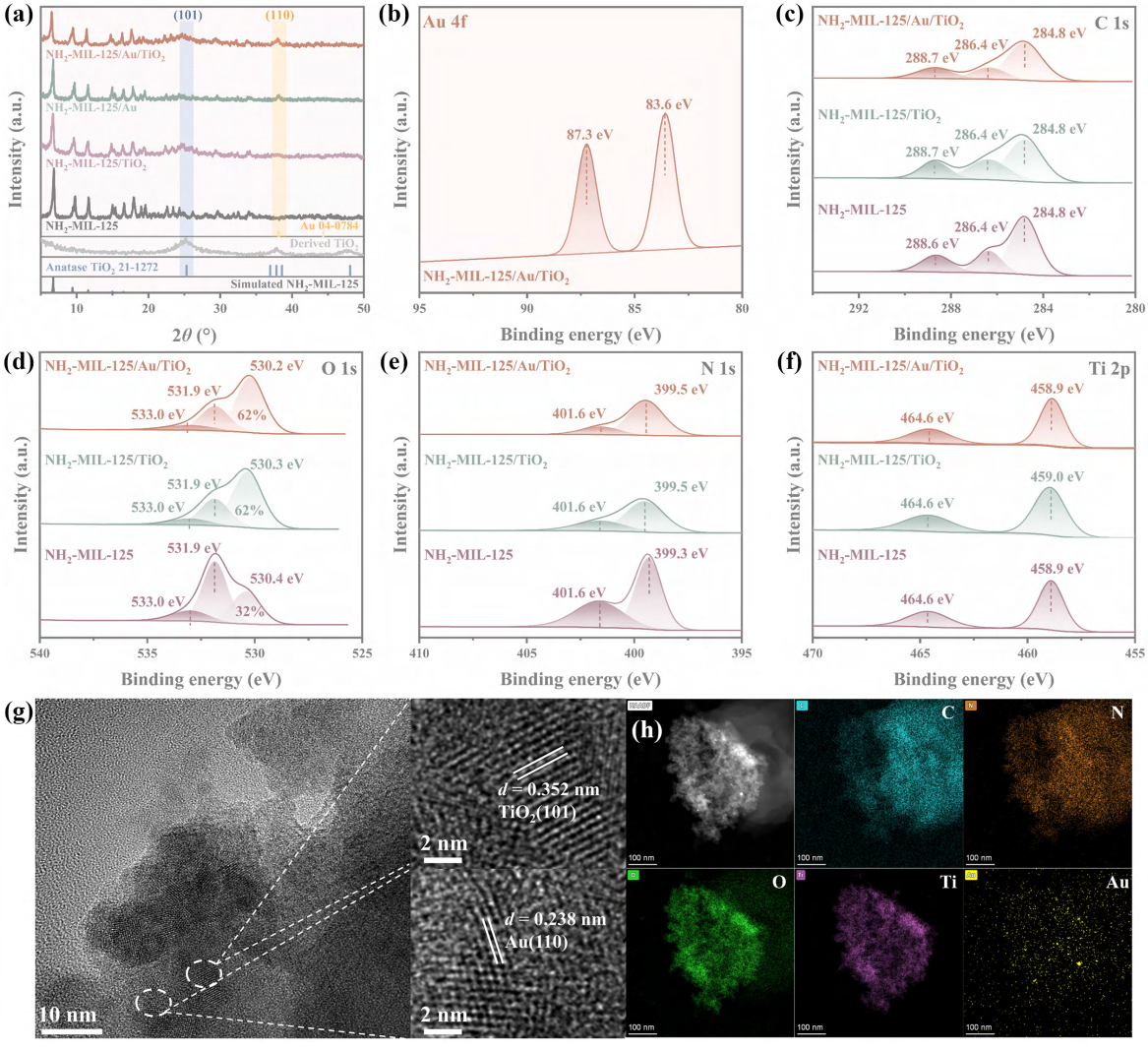

Figure 1 (a) The XRD spectra of simulated NH_2-MIL-125, anatase TiO_2, derived TiO_2, Au, NH_2-MIL-125, NH_2-MIL-125/TiO_2, NH_2-MIL-125/Au, and NH_2-MIL-125/Au/TiO_2. (b) Au 4f spectrum of NH_2-MIL-125/Au/TiO_2. (c) C 1s, (d) O 1s, (e) N 1s, and (f) Ti 2p spectra of NH_2-MIL-125, NH_2-MIL-125/TiO_2, and NH_2-MIL-125/Au/TiO_2. (g) TEM image and (h) EDS mapping of NH_2-MIL-125/Au/TiO_2.

analysis of NH_2-MIL-125/TiO_2 reveals complete retention of the parent MOFs's crystalline structure, along with the appearance of a distinct diffraction signal at 25.3° assignable to anatase TiO_2 [30]. Furthermore, prior to TiO_2 *in-situ* deposition, the Au NPs are introduced onto NH_2-MIL-125. The XRD analysis of NH_2-MIL-125/Au reveals an additional diffraction peak at 38.1°, which is indexed to the (111) plane of Au NPs [14], providing unambiguous evidence for the successful incorporation of Au. When TiO_2 NPs are subsequently *in-situ* grown within the Au-modified MOF matrix, the resulting ternary NH_2-MIL-125/Au/TiO_2 retains all primary characteristic peaks of NH_2-MIL-125/Au, though a slight reduction in peak intensity is observed after hydrothermal treatment. Notably, a prominent new diffraction peak appeared at 25.3°, which is assigned to the anatase TiO_2. The coexistence of NH_2-MIL-125, Au, and TiO_2 confirms the successful construction of a ternary composite while maintains the structural stability of the overall MOFs.

To further elucidate the chemical components and structural integrity of samples, FT-IR was carried out. The FT-IR spectra of both NH_2-MIL-125/Au/TiO_2 and NH_2-MIL-125/TiO_2 match the parent MOFs (Fig. S1 in the ESM), establishing that neither TiO_2 nor Au incorporation compromises the MOF overall structural integrity. The characteristic peaks observed at 1360–1580 cm^{-1} correspond to the symmetric (1572 and 1537 cm^{-1}) and asymmetric (1380 and 1424 cm^{-1}) stretching vibrations of the carboxylate groups (–COOH) [31], while the peaks at 1255 and 1624 cm^{-1} are attributed to the C–N stretching vibrations [32]. Additionally, the vibration modes of Ti-oxo clusters are identified within the range of 500–800 cm^{-1} (767, 628, and 540 cm^{-1}) [33]. Vibrational spectroscopy reveals attenuated –COOH band intensities in the NH_2-MIL-125/Au/TiO_2 relative to the unmodified MOFs, suggesting partial ligand dissociation during hydrolysis [34]. The partial removal of organic ligands leads to the exposure of Ti-oxo species, which serve as active sites for the hydrolytic formation of TiO_2 nanoparticles [28]. To further investigate the thermal stability and composition change, thermogravimetric analysis (TGA) was performed (Fig. S2 in the ESM), and the weight loss associated with NH_2-BDC ligands in pristine NH_2-MIL-125 was approximately 39.54%, whereas this value decreased to 34.75% for NH_2-MIL-125/Au/TiO_2. This observation is in line with the partial degradation of NH_2-BDC ligands noted.

XPS was employed to analyze the chemical composition and electronic states of samples. The survey spectra (Fig. S3 in the ESM) reveal distinct signals for C, N, O, and Ti in all samples. Notably, additional characteristic peak corresponding to Au element is clearly observed in the full spectrum of NH_2-MIL-125/Au/TiO_2. High-resolution XPS analysis of the Au 4f region (Fig. 1(b)) displays characteristic doublet peaks at 83.6 and 87.3 eV, confirming the presence of metallic Au^0 within the NH_2-MIL-125/Au/TiO_2 [35, 36]. High-resolution XPS analysis of the C 1s region (Fig. 1(c)) identifies characteristic components at 284.8 (C–C), 286.4 (C–N), and 288.6 eV (C=O) [37]. Upon modification, while the C–C and C–N peaks remain stable, the carboxyl carbon peak exhibits a systematic positive shift, indicating altered electronic environments. The O 1s XPS analysis (Fig. 1(d)) reveals three oxygen environments characteristic of Ti–O bonds (530.4 eV), C=O (531.9 eV), and terminal hydroxyls (533.0 eV) in NH_2-MIL-125 [28]. The O 1s spectra of NH_2-MIL-125/TiO_2 and NH_2-MIL-125/Au/TiO_2 exhibit significant changes, especially the content of Ti–O bonds increasing markedly compared to that of the pristine NH_2-MIL-125, rising from 32% to 62%, which is attributed to the *in-situ* formation of TiO_2. Additionally, a slight shift toward lower binding energy can be observed in the Ti–O peak position. The high-resolution N 1s spectra (Fig. 1(e)) reveal two characteristic nitrogen states: amino ligand (–NH_2) at 399.3 eV and protonated species (–N^+ or –NH–$^+$) at 401.6 eV in NH_2-MIL-125 [34, 38]. In the functionalized composites, these peaks exhibit both intensity reduction and positive binding energy shifts (–NH_2), which may be attributed to the detachment of NH_2-BDC ligands during metal oxide formation. The Ti 2p spectra (Fig. 1(f)) exhibit characteristic doublet peaks at 458.9 (2 $p_{3/2}$) and 464.6 eV (2 $p_{1/2}$), confirming the presence of Ti^{4+} species in the prepared materials [39, 40]. Overall, compared with the pristine MOFs, the peaks primarily assigned to NH_2-MIL-125 exhibit a general shift toward higher binding energy, while those mainly attributed to TiO_2 show a trend toward lower binding energy, providing the evidence for electron density redistribution between TiO_2 and NH_2-MIL-125 [14].

Sample morphology was characterized by scanning electron microscopy (SEM). NH_2-MIL-125 (Fig. S4(a) in the ESM) showcases a polished surface topography, consistent with findings in the existing scholarly literature [41]. In contrast, the successful integration of either uniformly dispersed TiO_2 (Fig. S4(b) in the ESM) or Au (Fig. S5(a) in the ESM) into NH_2-MIL-125 leads to a notable increase in surface roughness [42]. For comparative purposes, Au NPs are also immobilized on NH_2-MIL-125/TiO_2 to create NH_2-MIL-125/TiO_2/Au (Fig. S5(b) in the ESM) with further analogous surface roughness compared to NH_2-MIL-125/TiO_2 alone. Furthermore, after the *in-situ* growth of TiO_2 within NH_2-MIL-125/Au, the resulting ternary NH_2-MIL-125/Au/TiO_2 (Fig. S4(c) in the ESM) maintains a similar overall morphology to NH_2-MIL-125/Au while exhibiting even more pronounced surface texture. To further verify the structural information of NH_2-MIL-125/Au/TiO_2, high-resolution transmission electron microscopy (HRTEM) was conducted. The lattice spacing analyses (Fig. 1(g) and Fig. S6 in the ESM) reveal distinct crystallographic features: The measured interplanar spacing of 0.352 nm corresponds to the (101) crystal plane of anatase TiO_2 [43], while the interplanar spacing of 0.238 nm is attributed to the (111) crystal plane of Au NPs [44]. The results conclusively demonstrate the co-presence of TiO_2 and Au NPs in the NH_2-MIL-125/Au/TiO_2 composite. Energy-dispersive X-ray spectroscopy (EDS) (Fig. 1(h)) verifies the elemental composition, revealing distinct signals for C, N, O, Ti, and Au, which corroborated the successful synthesis of the ternary NH_2-MIL-125/Au/TiO_2 system.

To elucidate the combined influence of interface architecture and Au NPs mediation, we conducted DFT calculations. Based on the classic type-II heterojunction, once the NH_2-MIL-125 forms a heterojunction with TiO_2, electrons spontaneously transfer from NH_2-MIL-125's conduction band to TiO_2's conduction band due to NH_2-MIL-125's more negative conduction band position compared to TiO_2. As we expected, at the NH_2-MIL-125/TiO_2 heterojunction, the calculations of the differential charge density distribution (Fig. 2(a)) and the planar average differential charge (Fig. 2(b)) indicate that TiO_2 tends to gain electrons while NH_2-MIL-125 tends to lose electrons when the heterojunction is formed. While type-II heterojunctions effectively separate charge carriers, this configuration inherently compromises the redox potential of the photocatalytic system. However, in fact, the NH_2-MIL-125/Au/TiO_2 exhibits stronger ability to ROS. This is likely due to the introduction of Au NPs, which alters the charge transfer direction

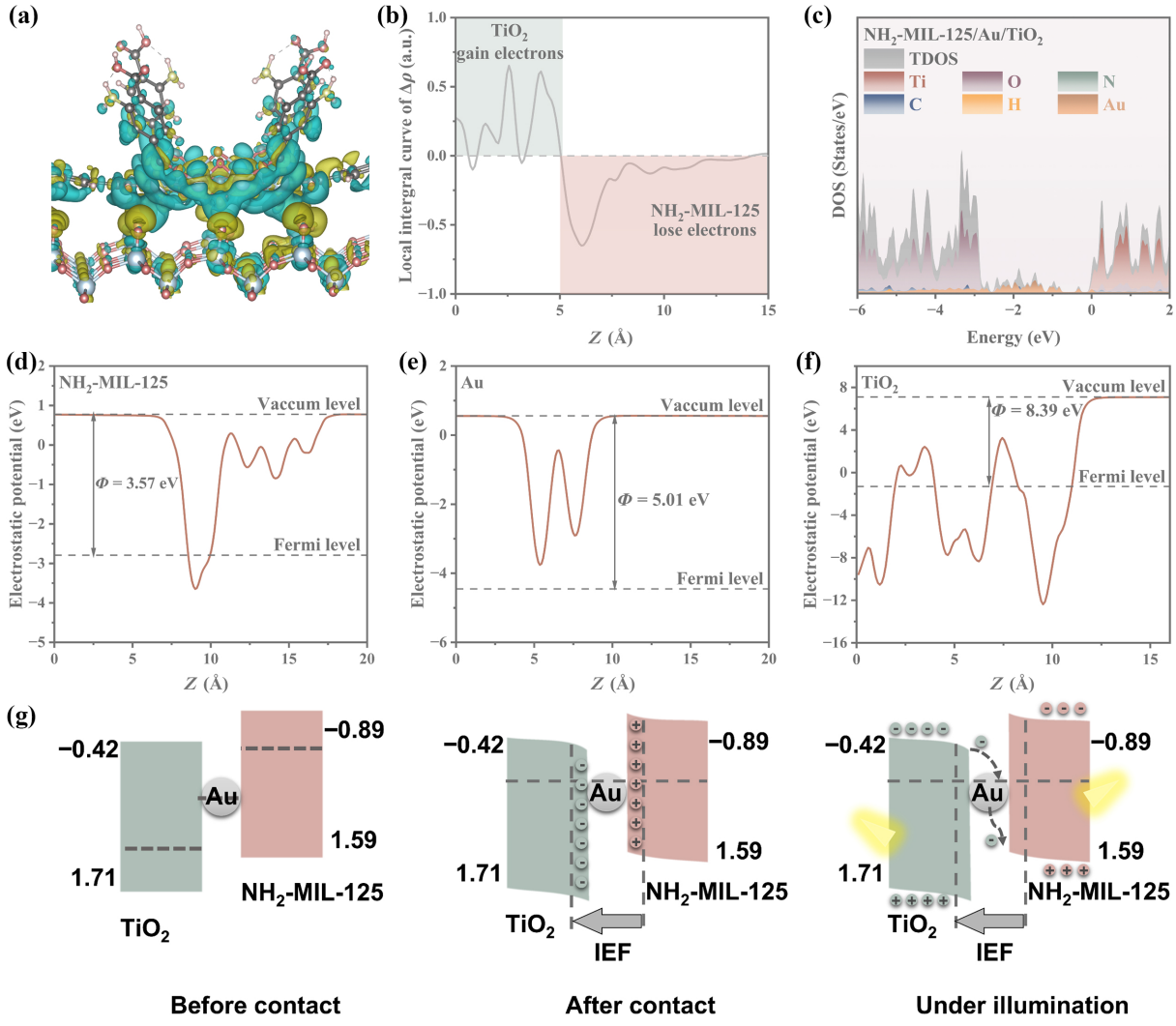

Figure 2 (a) Differential charge density distribution, (b) two-dimensional plane differential charge, and (c) density of states of NH_2-MIL-125/Au/TiO_2. ((d)–(f)) Work functions of (d) NH_2-MIL-125, (e) Au, and (f) TiO_2. (g) Electron migration route of Z-scheme heterojunction of NH_2-MIL-125/Au/TiO_2.

of the heterojunction, leading to a possible transformation in the heterojunction type [45]. By calculating the density of states (DOS) of NH_2-MIL-125/TiO_2 and NH_2-MIL-125/Au/TiO_2, we gain insights into the band structures of the heterojunction (Fig. 2(c) and Fig. S7 in the ESM). The conduction bands (CB) of both NH_2-MIL-125/TiO_2 and NH_2-MIL-125/Au/TiO_2 are primarily contributed by Ti, while the valence bands (VB) are mainly contributed by O. Notably, the introduction of Au leads to additional energy bands in NH_2-MIL-125/Au/TiO_2 that overlap with the conduction and valence bands of the heterojunction, indicating that the Au NPs cause a redistribution of electrons and bridge the NH_2-MIL-125 and TiO_2, facilitating enhanced interfacial charge transfer [14].

Additionally, work functions (WF) for NH_2-MIL-125, Au, and TiO_2 (Figs. 2(d)–2(f)) reveal interfacial energy alignment critical for charge transfer dynamics in the heterojunction system. NH_2-MIL-125, Au, and TiO_2 show gradually increasing WF, which are 3.57, 5.01, and 8.39 eV, respectively [14, 46, 47], establishing a unidirectional electron transfer gradient. Therefore, in the NH_2-MIL-125/Au/TiO_2 heterojunction, electrons from the conduction band of NH_2-MIL-125 spontaneously transfer to Au, and the electrons on Au further transfer to the valence band of TiO_2 until achieving Fermi level alignment across the three components. The introduction of Au NPs leads to a redistribution of charge, bringing out an increase in the electron density of TiO_2 and a decrease in the electron density of NH_2-MIL-125, forming a built-in electric field (IEF) of NH_2-MIL-125 pointing towards TiO_2. The following *in-situ* XPS results of NH_2-MIL-125/Au/TiO_2 demonstrate that photogenerated electrons in TiO_2's conduction band migrate toward NH_2-MIL-125's valence band under the IEF, where they recombine with holes of NH_2-MIL-125. This Z-scheme charge transfer mechanism effectively preserves the photogenerated electrons on NH_2-MIL-125 and photogenerated holes on TiO_2, allowing their participation in subsequent photocatalytic reactions, maintaining strong redox potentials while achieving spatial charge separation (Fig. 2(g)).

To further investigate the charge transfer process within the samples, the femtosecond transient absorption (fs-TA) spectroscopy was employed. As shown in Fig. S9(a) in the ESM, the pristine NH_2-MIL-125 exhibits an excited-state absorption (ESA) signal at 610 nm, which can be attributed to the ligand-to-metal charge transfer (LMCT) effect. The NH_2-MIL-125/TiO_2 (Fig. 3(a)) displays a similar ESA signal but with significantly enhanced intensity. Notably, the ternary NH_2-MIL-125/Au/TiO_2 exhibits distinct ESA features (Fig. 3(b)), with double ESA signals observed

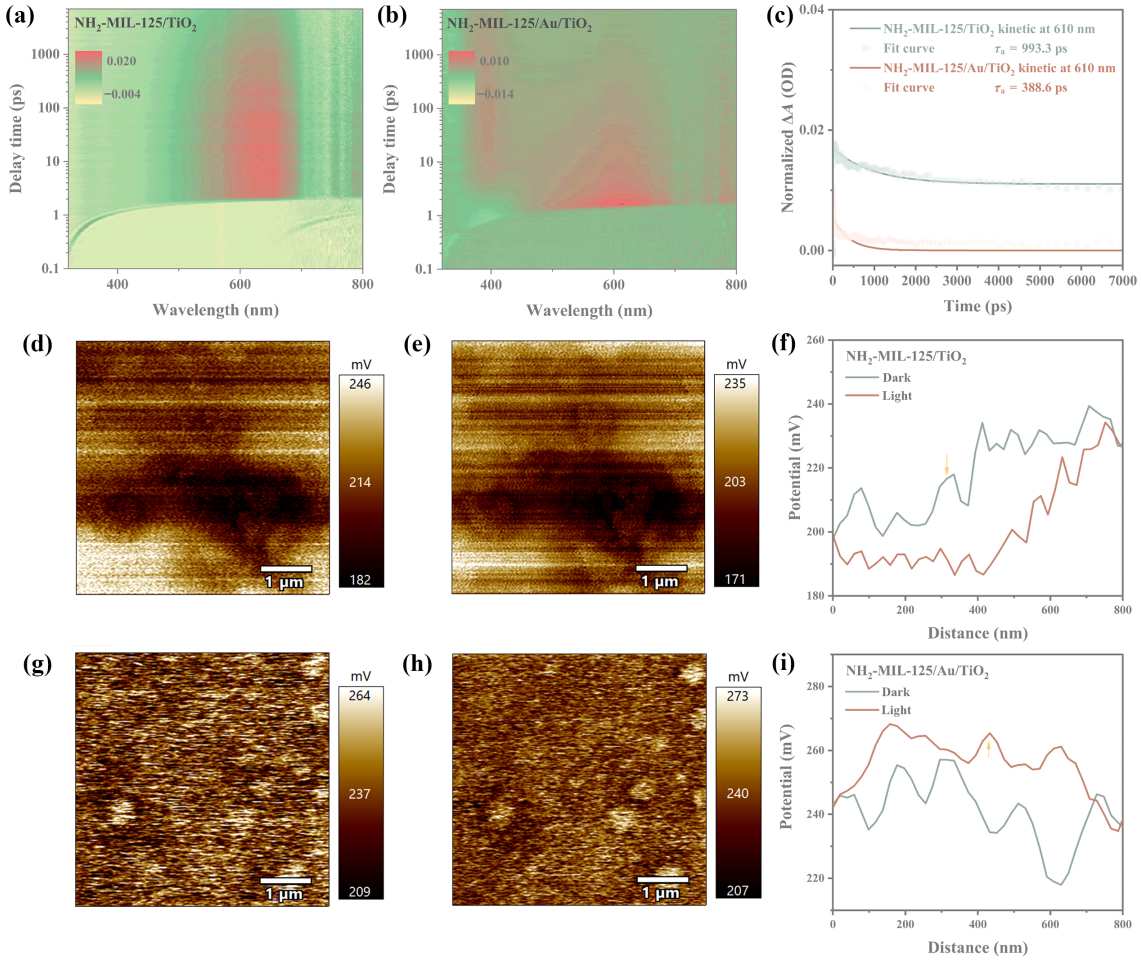

Figure 3 ((a) and (b)) The fs-TA spectra of (a) NH_2-MIL-125/TiO_2 and (b) NH_2-MIL-125/Au/TiO_2. (c) Normalized fs-TA decay curves of NH_2-MIL-125/TiO_2 and NH_2-MIL-125/Au/TiO_2 at 610 nm. ((d)–(i)) The KPFM potential images in the dark, under irradiation, and surface potential spectra of ((d)–(f)) NH_2-MIL-125/TiO_2 and ((g)–(i)) NH_2-MIL-125/Au/TiO_2.

around 390 and 610 nm, and a broader spectral response. Furthermore, the temporal evolution of the transient absorption spectra is monitored at 610 nm for the three samples. As shown in Figs. S9(b) and S9(c) in the ESM, NH_2-MIL-125 and NH_2-MIL-125/TiO_2 exhibit similar spectral profiles, both featuring a ground-state bleach (GSB) signal at around 315 nm and an ESA signal near 610 nm. The more obvious ESA signal in NH_2-MIL-125/TiO_2 suggests that the type-II heterojunction effectively facilitates the separation of photogenerated charge carriers. In addition, NH_2-MIL-125/Au/TiO_2 (Fig. S9(d) in the ESM) displays a distinct additional ESA signal at 390 nm, which may be attributed to the generation of hot electrons via the plasmonic effect of Au nanoparticles. Simultaneously, Au serves as an electron bridge between TiO_2 and NH_2-MIL-125, enabling the recombination of photogenerated electrons from TiO_2 with holes from NH_2-MIL-125. Moreover, a more intense GSB signal is observed, indicating a higher yield of photogenerated charge carriers in the NH_2-MIL-125/Au/TiO_2 system. The normalized fs-TA decay curves (Fig. 3(c)) indicate that the NH_2-MIL-125/Au/TiO_2 Z-scheme heterojunction decays more rapidly compared to the type-II NH_2-MIL-125/TiO_2 heterojunction. Time-resolved photoluminescence (TRPL) spectroscopy (Fig. S9(e) in the ESM) further supports this finding, in which the Z-scheme NH_2-MIL-125/Au/TiO_2 exhibits the short photoluminescence lifetime in comparison to the type-II NH_2-MIL-125/TiO_2. These results collectively demonstrate the more fast and efficient migration rate of photogenerated charge carriers in the Z-scheme heterojunction.

In addition, the Kelvin probe force microscopy (KPFM) was performed to examine the surface potential distribution of the heterojunction before and after light irradiation. For NH_2-MIL-125/TiO_2 (Figs. 3(d)–3(f), and Figs. S9(f) and S9(g) in the ESM), the surface potential decreases significantly after illumination, indicating that TiO_2 in the type-II heterojunction gains electrons under light. In contrast, NH_2-MIL-125/Au/TiO_2 (Figs. 3(g)–3(i), and Figs. S9(h) and S9(i) in the ESM) shows a certain increase in surface potential after illumination, suggesting that TiO_2 in the Z-scheme heterojunction tends to lose electrons. The obviously opposite behavior further corroborates the distinct charge transfer pathways in the two types of heterojunctions.

3.2 Photocatalytic NO removal

Assessment of photocatalytic NO oxidation under visible light reveals a removal rate of 22.1% for pristine NH_2-MIL-125 (Fig. 4(a)). Remarkable enhancements were achieved through strategic modifications, and the introduction of either TiO_2 or Au NPs individually boosts the NO removal efficiency to 67.3% and 63.8% for NH_2-MIL-125/TiO_2 and NH_2-MIL-125/Au, respectively. These significant improvements demonstrate that both the

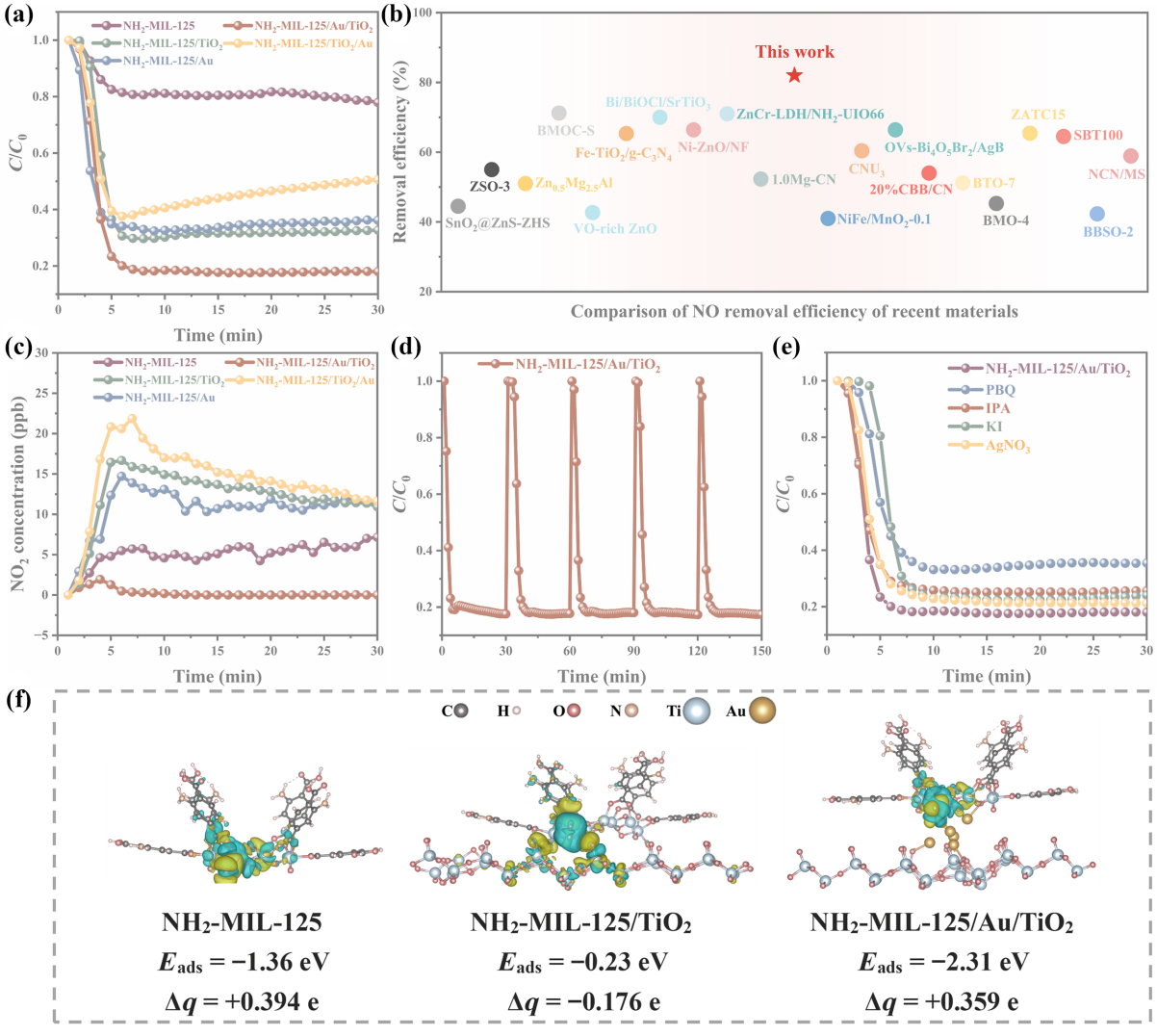

Figure 4 (a) The NO removal efficiency and (c) the corresponding NO_2 production of NH_2-MIL-125, NH_2-MIL-125/TiO_2, NH_2-MIL-125/Au, NH_2-MIL-125/Au/TiO_2, and NH_2-MIL-125/TiO_2/Au. (b) The comparison of the photocatalytic NO removal rate with of other photocatalysts. (d) NO removal efficiency under 5 consecutive experiments. (e) The free radical capture experiments of NH_2-MIL-125/Au/TiO_2. (f) NO molecule interactions with NH_2-MIL-125, NH_2-MIL-125/TiO_2, and NH_2-MIL-125/Au/TiO_2.

formation of a type-II heterojunction through *in-situ* TiO_2 incorporation and the introduction of Au NPs can substantially enhance the photocatalytic performance. However, first constructing NH_2-MIL-125/TiO_2 heterojunction followed by Au deposition results in inferior photocatalytic NO removal efficiency (49.4%). This obvious decrease may be attributed to that the Au NPs blocked almost all the NH_2-MIL-125/TiO_2's micropores (as shown in Table S3 and Fig. S10 in the ESM), thereby significantly reducing its specific surface area. During the NO removal process, the adsorption–desorption equilibrium is first achieved under dark conditions. When the samples possess insufficient specific surface area and active sites, this situation leads to an initial increase in removal efficiency followed by a gradual decline over time. In dramatic contrast, the Z-scheme NH_2-MIL-125/Au/TiO_2, fabricated by *in-situ* TiO_2 growth on pre-deposited Au-modified NH_2-MIL-125, achieves an exceptional NO removal efficiency (82.0%). This exceptional performance originates from the precisely controlled architecture, where Au NPs are positioned as interfacial bridges between NH_2-MIL-125 and TiO_2, enabling efficient charge transfer across the Z-scheme heterojunction. Furthermore, this system demonstrates superior NO removal performance compared to other photocatalysts (Fig. 4(b) and Table S4 in the ESM).

While evaluating NO degradation, we monitored the generation of NO_2, a toxic byproduct. The NO_2 production levels (Fig. 4(c)) for original NH_2-MIL-125, NH_2-MIL-125/TiO_2, NH_2-MIL-125/Au, and NH_2-MIL-125/TiO_2/Au are remarkably low (< 25 ppb), accounting for only 5% of the initial NO concentration (550 ppb). Of particular significance, the NH_2-MIL-125/Au/TiO_2 not only achieves an exceptional NO removal efficiency of 82.0% but also exhibits the lowest NO_2 production levels among all tested samples. During the photocatalytic reaction, the NH_2-MIL-125/Au/TiO_2 exhibits only minimal NO_2 generation during initial reaction stages, with the NO_2 concentration dropping to almost 0 ppb in subsequent stages. The result demonstrates that NH_2-MIL-125/Au/TiO_2 effectively avoids the generation of secondary toxic pollutants during NO removal. Instead, it predominantly converts NO into harmless nitrate and nitrite species, achieving 100% selectivity toward NO_2^-/NO_3^- after 30 min of reaction. To further verify the stability of

the NO purification efficiency and the structural integrity of NH_2-MIL-125/Au/TiO_2, we conducted five consecutive NO purification cycle experiments. The NH_2-MIL-125/Au/TiO_2 exhibits outstanding stability in NO removal, maintaining a removal efficiency consistently above 82.0% over five cycles (Fig. 4(d)). Moreover, only trace amounts of NO_2 secondary pollutants (< 5 ppb) are detected during the initial min of each cycle (Fig. S11(a) in the ESM), with subsequent concentrations of NO_2 secondary contaminants consistently at 0 ppb, confirming the material's capability for deep and long-term NO oxidation. Additionally, XRD and SEM analyses reveal no significant changes in its crystal structure or morphology of NH_2-MIL-125/Au/TiO_2 after cycling tests (Figs. S11(b)–S11(d) in the ESM), further supporting its potential as a stable and efficient photocatalyst. To elucidate the reactive species involved in NO photo-oxidation over NH_2-MIL-125/Au/TiO_2, radical trapping experiments were performed. As depicted in Fig. 4(e), the introduction of specific scavengers suppresses the reaction efficiency, indicating the participation of multiple radicals in the photocatalytic process. Notably, the photocatalytic efficiency decreases most significantly when benzoquinone (PBQ), a trapping agent for $\cdot O_2^-$, is added. This result indicates that the $\cdot O_2^-$ is the primary active free radical in the NH_2-MIL-125/Au/TiO_2 system.

Through the DFT calculations, the interaction capability between NO and the samples was also elucidated (Fig. 4(f)). The adsorption energies of NO for NH_2-MIL-125, NH_2-MIL-125/TiO_2, and NH_2-MIL-125/Au/TiO_2 are −1.36, −0.23, and −2.31 eV, respectively. The Bader charges between NO and NH_2-MIL-125, NH_2-MIL-125/TiO_2, and NH_2-MIL-125/Au/TiO_2 are +0.394 e, −0.176 e, and +0.359 e, respectively. Of particular significance is that NH_2-MIL-125/Au/TiO_2 exhibits more negative adsorption energy, indicating a more convenient interaction ability with NO, which is favorable for NO removal [48]. In the NH_2-MIL-125/Au/TiO_2 Z-scheme system, the NO molecule tends to gain electrons, facilitating the formation of the NO^- intermediate and optimizing the NO reaction pathway. In contrast, in the NH_2-MIL-125/TiO_2 type-II system, the NO molecule tends to lose electrons via oxidation to obtain NO^+ intermediate.

3.3 The possible photocatalytic NO removal mechanism

The trapping experiments confirm that $\cdot O_2^-$ and ·OH play a significant role in the photocatalytic oxidation of NO, with high contribution rates of 21.27% and 11.83%, respectively (Fig. 5(a)). To directly detect the active free radicals generated during the photocatalytic reaction, we employed electron paramagnetic resonance (EPR) spectroscopy to analyze NH_2-MIL-125/TiO_2 and

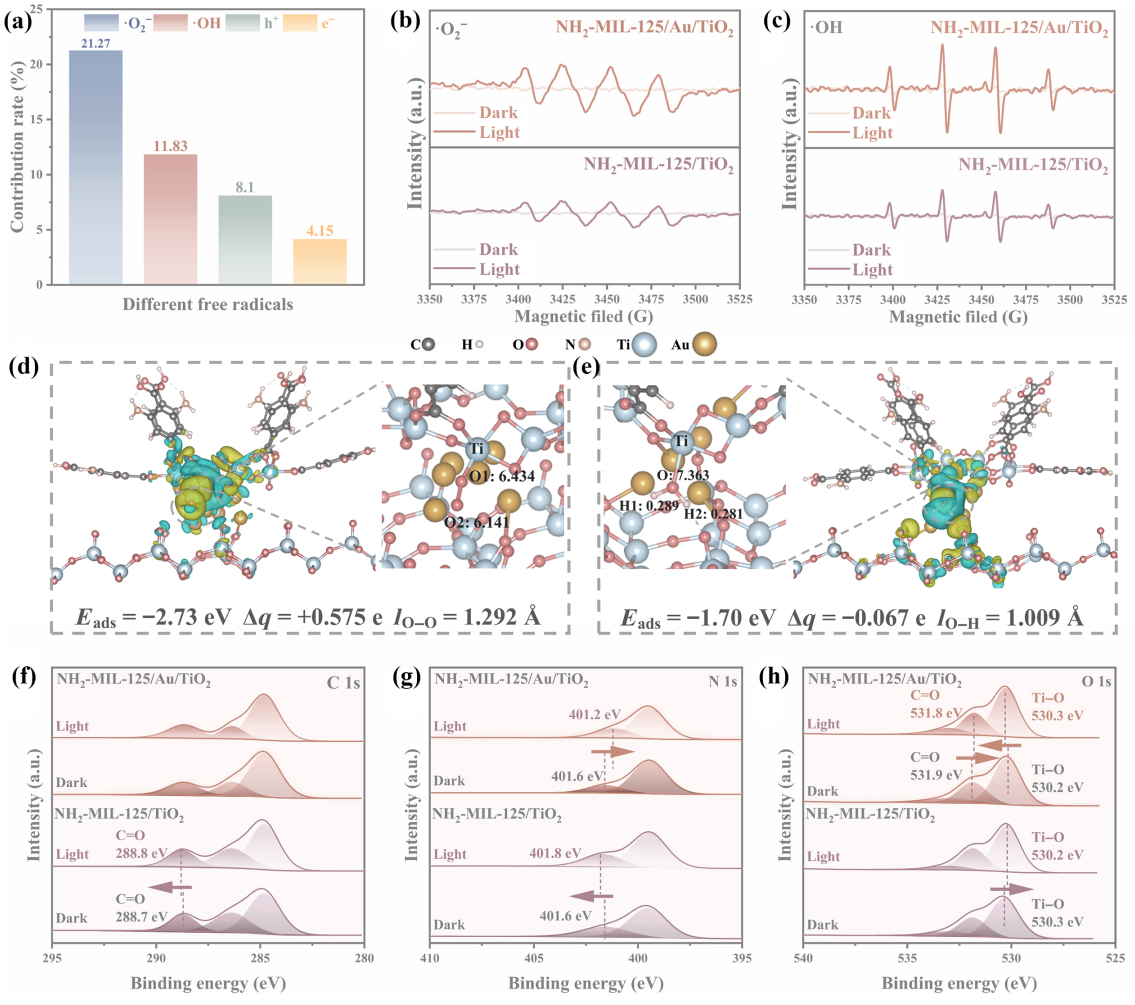

Figure 5 (a) The contribution rates of each free radical in NO removal of NH_2-MIL-125/Au/TiO_2. ((b) and (c)) EPR detection under darkness and light (b) $\cdot O_2^-$ and (c) ·OH of NH_2-MIL-125/TiO_2 and NH_2-MIL-125/Au/TiO_2. ((d) and (e)) The adsorption and activation capabilities and bader charge analysis of NH_2-MIL-125/Au/TiO_2 for small molecule (d) O_2 and (e) H_2O. (f) C 1s, (g) N 1s, and (h) O 1s *in-situ* illuminated XPS spectra of NH_2-MIL-125/TiO_2 and NH_2-MIL-125/Au/TiO_2.

NH_2-MIL-125/Au/TiO_2 (Figs. 5(b) and 5(c)). EPR is a highly sensitive technique capable of directly detecting and identifying free radicals, particularly under light irradiation, where signals of radicals such as $\cdot O_2^-$ and ·OH can be captured in real time. Under dark conditions, almost no free radical signals are detected, however, under light irradiation, both NH_2-MIL-125/TiO_2 and NH_2-MIL-125/Au/TiO_2 exhibit intense signals, with a characteristic intensity ratio of 1:1:1:1 for $\cdot O_2^-$ and 1:2:2:1 for ·OH. Notably, the signal intensities of $\cdot O_2^-$ and ·OH generated by NH_2-MIL-125/Au/TiO_2 are significantly stronger than those of NH_2-MIL-125/TiO_2. This enhancement originates from Au NPs' dual functionality, mediating interfacial electron transport between semiconductor and MOF components and generating localized surface plasmon resonance (LSPR)-induced hot carriers that boost radical formation through improved charge separation.

To investigate the generation of ROS, we employed DFT calculations to examine the adsorption and activation capabilities of samples toward O_2 and H_2O. The adsorption energies (E_{ads}) (Fig. 5(d) and Fig. S14 in the ESM) of O_2 on NH_2-MIL-125, NH_2-MIL-125/TiO_2, and NH_2-MIL-125/Au/TiO_2 are −1.27, −1.55, and −2.73 eV, respectively. In the O_2 system for NH_2-MIL-125/Au/TiO_2, the O_2 molecules tend to gain electrons and display the longest O–O bond length, facilitating the reduction to obtain $\cdot O_2^-$. At the same time, the corresponding adsorption energies for H_2O are −0.75, −1.66, and −1.70 eV, respectively. Simultaneously, in the H_2O system for NH_2-MIL-125/Au/TiO_2 (Fig. 5(e)), the H_2O molecules more easily lose electrons, and the longest O–H bond length is beneficial to the O–H bond cleavage for H^+ generation, promoting the evolution from H_2O_2 to ·OH [49]. The E_{ads} of O_2 and H_2O clearly demonstrate the spontaneous adsorption ability for both O_2 and H_2O on all samples, in which the NH_2-MIL-125/Au/TiO_2 exhibits more negative adsorption energy, indicating that NH_2-MIL-125/Au/TiO_2 more readily adsorbs and activates O_2 and H_2O molecules [50]. Furthermore, we analyzed the bond interaction and electron transfer situation between the photocatalysts and small molecules through combined electron localization function (ELF) and Bader charge values (Fig. S15 in the ESM). During the O_2 and H_2O activation process, obvious interactions occur between the photocatalysts and small molecules, in which the NH_2-MIL-125/Au/TiO_2 also exhibits the superior interactions with O_2 and H_2O that significantly contributed to the generation of ROS.

In-situ XPS analysis was conducted to monitor the charge dynamics before and after light irradiation, which provides direct experimental evidence of the charge transfer direction for photocatalyst during the photocatalytic process. Light-irradiated *in-situ* XPS characterization of NH_2-MIL-125/TiO_2 demonstrates binding energy changes, and the carboxyl group C=O (Fig. 5(f)) and amino group N (Fig. 5(g)) peaks exhibit positive shifts of +0.1 and +0.2 eV, respectively. Concurrently, the Ti–O bond (Fig. 5(h)) exhibits a shift toward lower binding energy. The previous XPS analysis (Fig. 1(f)) reveals that the formation of TiO_2 significantly alters the O 1s spectrum, with a substantial increase in Ti–O bond content, confirming that the Ti–O bond primarily originated from TiO_2. After illumination, the peaks associated with NH_2-MIL-125 shift to higher binding energy, while those related to TiO_2 shift to lower values, indicating that photogenerated electrons migrate from NH_2-MIL-125 to TiO_2 during the photocatalytic reaction, consistent with the charge transfer pathway of a type-II heterojunction. Conversely, the *in-situ* XPS spectra of NH_2-MIL-125/Au/TiO_2 exhibit an opposite trend after illumination, and the peaks corresponding to the amino and carboxyl groups of NH_2-MIL-125 decrease toward lower binding energy, while those associated with TiO_2 increase toward higher binding energy, suggesting that photogenerated electrons transfer from TiO_2 to NH_2-MIL-125 during the photocatalytic process, demonstrating the typical photoinduced carrier transfer featured of Z-scheme photocatalytic systems.

In-situ FT-IR tracks the evolution of intermediates and final products during sequential dark adsorption and light irradiation phases. Figure 6(a) and Fig. S16(a) in the ESM present the spectral evolution during NO adsorption and photocatalytic conversion over NH_2-MIL-125. Remarkably similar infrared spectra are observed between dark adsorption and visible light irradiation conditions. Characteristic absorption peaks at 1049, 1078, and 1639 cm^{-1} confirm NO adsorption on NH_2-MIL-125. Additional peaks at 907, 948, and 1724 cm^{-1} are identified as NO_2 (948 cm^{-1}) and N_2O_4 (948 and 1724 cm^{-1}), suggesting that NO preferentially reacted with O_2 to form these toxic byproducts because of the limited oxidative potential of the NH_2-MIL-125. The reversible NO_2/N_2O_4 equilibrium is clearly observed. Simultaneously, a characteristic peak at 1163 cm^{-1} is detected, assigning to NO^-, an ideal reaction intermediate formed through electron acquisition by NO molecules. Furthermore, distinct peaks at 1362, 1400, 1500, and 1590 cm^{-1} corresponding to nitrite (1500 and 1590 cm^{-1}) and nitrate species (1362 and 1400 cm^{-1}) are detected under both dark and light conditions, indicating partial NO oxidation by NH_2-MIL-125. The NH_2-MIL-125/TiO_2 system exhibits nearly identical FT-IR spectra under dark and illuminated conditions (Fig. 6(b) and Fig. S16(b) in the ESM), with characteristic peaks for NO (1639 cm^{-1}), NO_2 (838, 885, 920, and 939 cm^{-1}), N_2O_4 (1724 cm^{-1}), and NO^+ (1689 cm^{-1}) clearly visible. Obvious vibrational modes corresponding to nitrite (1500 and 1590 cm^{-1}) and nitrate (1044, 1362, and 1411 cm^{-1}) are also observed. After illumination, the peak of NO weakens (1639 cm^{-1}) and the peak of NO_3^- strengthens (1362 and 1411 cm^{-1}), indicating the enhancement of photocatalytic activity. Figure S16(c) in the ESM shows the spectral evolution during dark NO adsorption of NH_2-MIL-125/Au/TiO_2. The characteristic NO peak at 1639 cm^{-1} intensifies, accompanied by the appearance of NO^- (1158 cm^{-1}) signatures. Nitrite species (860, 1500, and 1590 cm^{-1}) and nitrate species (1362 and 1400 cm^{-1}) are also detected. After light irradiation (Fig. 6(c)), the absorption peak of 1639 cm^{-1} weakens and the absorption intensities of NO_3^- (1362 cm^{-1}) increase substantially compared to dark conditions, confirming that visible light promotes deep NO oxidation over NH_2-MIL-125/Au/TiO_2.

The contour projection results during the photocatalytic reaction stage (Figs. 6(d)–6(f)) further reveal that NH_2-MIL-125 maintains a certain concentration level of NO while producing more NO_2^-. In contrast, both NH_2-MIL-125/TiO_2 and NH_2-MIL-125/Au/TiO_2 exhibit significantly greater NO_3^- formation, with NH_2-MIL-125/Au/TiO_2 demonstrating particularly pronounced NO_3^- accumulation over prolonged reaction time, clearly indicating its superior deep oxidation capability for NO conversion. The species corresponding to various peaks are listed in Tables S5–S7 in the ESM. The analysis of the corresponding contour plots reveals distinct photocatalytic behaviors, an the NH_2-MIL-125 primarily adsorbs NO with partial conversion to toxic NO_2 and minimal nitrate formation. The NH_2-MIL-125/TiO_2 shows improved NO oxidation capacity, generating more nitrite species but still limited nitrates, while the NH_2-MIL-125/Au/TiO_2 achieves the most

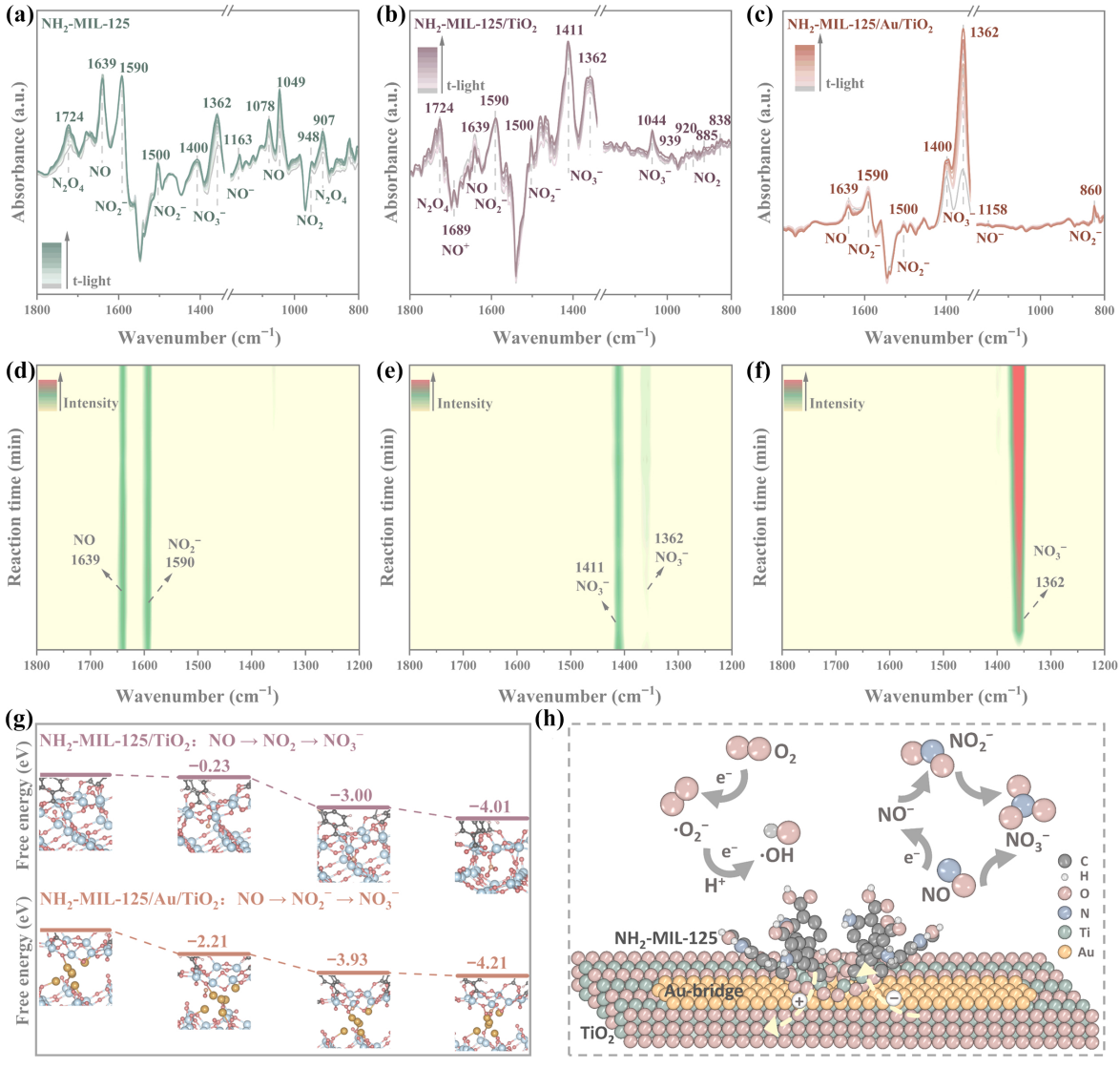

Figure 6 ((a)–(c)) *In-situ* FT-IR spectra of (a) NH_2-MIL-125, (b) NH_2-MIL-125/TiO_2, and (c) NH_2-MIL-125/Au/TiO_2 for NO removal under light irradiation conditions and ((d)–(f)) the corresponding contour projections for photocatalytic reaction. (g) The NO reaction path calculated for NH_2-MIL-125/TiO_2 and NH_2-MIL-125/Au/TiO_2. (h) The possible mechanism of NO removal by NH_2-MIL-125/Au/TiO_2.

complete NO oxidation, producing abundant nitrate species. The observed improvement likely stems from Au nanoparticles' dual roles, and beyond their plasmonic effects, they mediate the transition from type-II to Z-scheme heterojunction configuration. The heterojunction structure rearrangement dramatically improves the promotion of photogenerated charge carriers, collectively enhancing reactive oxygen species production and enabling deep pollutant oxidation. Specifically, the reaction pathways of NO in the NH_2-MIL-125/TiO_2 and NH_2-MIL-125/Au/TiO_2 systems are listed in Schemes S1 and S2 in the ESM.

Based on the distinct charge transfer mechanisms (Fig. S17 in the ESM) of NH_2-MIL-125/TiO_2 and NH_2-MIL-125/Au/TiO_2, their oxidative behaviors toward NO also differ significantly, leading to divergent reaction pathways (Fig. 6(g)). Specifically, in the type-II heterojunction NH_2-MIL-125/TiO_2, the limited reductive capability hinders electron gained by adsorbed NO molecules. Instead, it facilitates the formation of the NO^+ intermediate. The presence of this toxic intermediate impedes the deep oxidation of NO to NO_3^-, inevitably leading to the generation of incompletely oxidized NO_2 species during the photocatalytic process [49–51], as corroborated by our activity tests. Gibbs free energy analysis further confirms that NO is thermodynamically more favorable to oxidize into NO_2. Although NO_2 can be subsequently converted to NO_3^-, this stepwise oxidation pathway (NO → NO_2 → NO_3^-) results in substantial accumulation of toxic intermediates. In contrast, in the Z-scheme heterojunction NH_2-MIL-125/Au/TiO_2, which possesses strong reductive ability, NO readily gains electrons to generate NO^- species, effectively suppressing NO_2 formation [52], in agreement with the activity test results. The NO^- intermediate is predominantly formed and subsequently converted to NO_2^-, which is further oxidized to NO_3^- (NO → NO_2^- → NO_3^-). Notably, this reaction pathway exhibits a lower Gibbs free energy, indicating that NH_2-MIL-125/Au/TiO_2 promotes deeper oxidation of NO pollutants under photocatalytic conditions.

On the basis of comprehensive characterization and computational analysis, the proposed reaction mechanism for NH_2-MIL-125/Au/TiO_2 is schematically illustrated in Fig. 6(h). In this Z-scheme heterojunction system, the WF increase sequentially from

NH_2-MIL-125 to Au to TiO_2, while their Fermi levels decrease correspondingly. Upon formation of the heterojunction, electrons migrate spontaneously from NH_2-MIL-125 to Au and then to TiO_2, establishing an IEF directed toward TiO_2. Under light irradiation, photogenerated electrons in the conduction band of TiO_2 are driven by the IEF to recombine with the photoexcited holes localized in the valence band of NH_2-MIL-125. Within this Z-scheme architecture, the Au nanoparticles serve a dual role. They act as an electron bridge that alters the charge transfer pathway, facilitating spatial separation of photogenerated charge carriers, and they also exhibit an LSPR effect that enhances the photocatalytic activity. Importantly, this Z-scheme charge transfer dynamics preserves the strong reduction capability of NH_2-MIL-125.

Under visible light irradiation, NH_2-MIL-125/Au/TiO_2 is excited to generate electron–hole pairs (Eq. (S11) in the ESM). Owing to the Z-scheme mechanism, electrons accumulate on the conduction band of NH_2-MIL-125, which has sufficiently negative potential (–0.89 V) to reduce adsorbed O_2 to $\cdot O_2^-$ ($O_2/\cdot O_2^-$ (–0.33 V)) (Eq. (S12) in the ESM). The generated $\cdot O_2^-$ can further transform into ·OH (Eqs. (S13) and (S14) in the ESM). Both $\cdot O_2^-$ and ·OH serve as the primary reactive species in the subsequent photocatalytic oxidation process. In a continuous-flow NO reactor, the photocatalytic NO removal process initiates with molecular adsorption, where NO can react with electrons to form NO^- (Eq. (S15) in the ESM) or be directly oxidized by $\cdot O_2^-$ to NO_3^- (Eq. (S16) in the ESM). The intermediate products are further completely converted into nitrate and nitrite species under the action of active radicals (Eqs. (S17)–(S19) in the ESM).

4 Conclusions

In conclusion, through incorporation of Au NPs as electron bridges within *in-situ* fabricated NH_2-MIL-125/TiO_2, we successfully transformed the type-II heterojunction into Z-scheme heterojunction, enabling the regulation of the NO oxidation pathway and achieving efficient deep oxidation. Activity tests demonstrate that Z-scheme NH_2-MIL-125/Au/TiO_2 exhibits an impressive NO removal efficiency of 82.0%, surpassing the original NH_2-MIL-125 by 3.7 times and the type-II NH_2-MIL-125/TiO_2 by 1.2 times. Combining DFT calculations, fs-TA spectroscopy, and *in-situ* FT-IR, we identified that the superior performance of NH_2-MIL-125/Au/TiO_2 stems from the establishment of the Z-scheme heterojunction, which facilitates ROS generation and controls the NO reaction pathway. NH_2-MIL-125/Au/TiO_2 demonstrates enhanced adsorption and activation capabilities for O_2/H_2O molecules, promoting ROS production. Moreover, within the NH_2-MIL-125/Au/TiO_2 system, the NO^- intermediate product is preferentially generated, facilitating its deep oxidation to NO_3^-. This process effectively suppresses the formation of toxic by-products (NO_2 and NO^+) while regulating the rate-determining step of NO oxidation. This study aims to explore Au-mediated heterojunction transition from type-II to Z-Scheme to develop highly efficient and long-term stable MOFs-based photocatalysts for regulating the NO reaction pathway, offering significant implications for environmental purification.

Electronic Supplementary Material: Supplementary material (the chemical composition, morphological structure, photogenerated carrier separation ability, band structure of the photocatalysts, as well as NO removal activity tests, DFT calculations, *in-situ* FT-IR, etc.) is available in the online version of this article at https://doi.org/10.26599/NR.2026.94908660.

Data availability

All data needed to support the conclusions in the paper are presented in the manuscript and the Electronic Supplementary Material. Additional data related to this paper may be requested from the corresponding author upon request.

Acknowledgements

This work was supported by the National Natural Science Foundation of China (Nos. 22001026 and 52370109), the Natural Science Foundation Project of Chongqing (Nos. CSTB2025YITP-QCRCX0064, CSTB2025NSCQ-GPX0827, CSTB2024NSCQ-LZX0073, and CSTB2025NSCQ-GPX0816), and the Science and Technology Research Program of Chongqing Municipal Education Commission (Nos. KJZD-M202400802 and KJZD-K202300806).

Declaration of competing interest

All the contributing authors report no conflict of interest in this work.

Author contribution statement

X. Y. L.: Methodology, investigation, formal analysis, visualization, writing – original draft. K. L. W.: Methodology, investigation, validation, formal analysis, writing – original draft. Y. L.: Investigation, validation, visualization. Y. Z. H.: Formal analysis, investigation. Y. Y. F.: Formal analysis, writing – original draft, project administration, supervision. M. F.: Formal analysis. B. L.: Writing – original draft, conceptualization, project administration, supervision. Y. H. L.: Writing – original draft, conceptualization, project administration, supervision. All the authors have approved the final manuscript.

Use of AI statement

None.

References

[1] Chen, D. L.; Si, W. Z.; Yuan, X.; Peng, Y.; Li, J. H. Construction of dual-functional sites via Ru pre-loading on $(VO_x)_n/CeO_2$ for multi-pollutant control. *Nano Res.* **2026**, *19*, 94907975.

[2] Fan, X. X.; Teng, Z. Y.; Han, L. P.; Shen, Y. J.; Wang, X. Y.; Qu, W. Q.; Song, J. L.; Wang, Z. L.; Duan, H. Y.; Wu, Y. A. et al. Boosted charge and proton transfer over ternary $Co/Co_3O_4/CoB$ for electrochemical nitric oxide reduction to ammonia. *Nat. Commun.* **2025**, *16*, 4874.

[3] Esquivel-Elizondo, S.; Walkowiak, B.; Sartzetakis, S. S.; Buma, B. Climate impact of direct and indirect N_2O emissions from the ammonia marine fuel value chain. *Environ. Sci. Technol.* **2025**, *59*, 9037–9048.

[4] Shang, H.; He, Y.; Wang, Q.; Jia, H. B.; Wang, J. L.; Zhao, H. C.; Chen, X. W.; Deng, X. Y.; Zhang, Z. Y.; Gu, S. W. et al. Dual-active-site engineering via orbital modulation of Fe single atoms on defective TiO_2 for enhanced photocatalytic NO removal. *Nano Res.*, in press, DOI: 10.26599/NR.2025.94908244.

[5] Shi, X. Q.; Sun, Y. X.; Lai, K. Z.; Li, L. P.; Li, N.; Gao, Y. Q.; Ge, L. Mn induced adsorption and orbital hybridization synergistically

promote C–C coupling for highly selective photocatalytic CO_2-to-C_2H_4 conversion. *Appl. Catal. B: Environ. Energy* **2026**, *382*, 126001.

[6] Chen, P.; Ai, W. X.; Liu, H. J.; Ma, Y. R.; Dong, X.; He, W. J.; Liao, J. Z.; Wang, Y.; Zhang, W. D.; Dong, F. Cobalt–silver dual sites promote highly selective photocatalytic NO removal via synergy of internal electric field integrated plasmon and spin polarization effect. *J. Hazard. Mater.* **2026**, *501*, 140980.

[7] Li, K. L.; Wang, H.; Li, J. J.; Dong, F. Design and mechanism of photocatalytic oxidation for the removal of air pollutants: A review. *Environ. Chem. Lett.* **2022**, *20*, 2687–2708.

[8] Mu, J. C.; Zhou, M.; Wu, C.; Li, R.; Liu, B. J.; Zhang, J. J.; Yu, J. G.; Ho, W. Engineering Lewis basic sites in S-scheme heterostructure to boost deep photocatalytic oxidation of nitric oxides in air. *Appl. Catal. B: Environ. Energy* **2026**, *386*, 126388.

[9] Shang, H.; Jia, H. B.; Li, P. P.; Li, H.; Zhang, W. B.; Li, S. J.; Wang, Q.; Xiao, S. N.; Wang, D.; Li, G. S. et al. Highly selective and efficient photocatalytic NO removal: Charge carrier kinetics and interface molecular process. *Nano Res.* **2024**, *17*, 1003–1026.

[10] Li, N.; Wang, C. Y.; Zhang, K.; Lv, H. Q.; Yuan, M. Z.; Bahnemann, D. W. Progress and prospects of photocatalytic conversion of low-concentration NO_x. *Chin. J. Catal.* **2022**, *43*, 2363–2387.

[11] Wang, J. L.; Shen, S. J.; Li, X.; Li, J. Y.; Dong, F. Photoexcited active radicals for environmental and energy applications: Generation, regulation, and dynamic tracking. *Chem. Rev.* **2025**, *125*, 7811–7917.

[12] Dai, W. R.; Zhang, S.; Shang, H.; Xiao, S. N.; Tian, Z. L.; Fan, W. B.; Chen, X. L.; Wang, S. K.; Chen, W.; Zhang, D. Q. Breaking the selectivity barrier: Reactive oxygen species control in photocatalytic nitric oxide conversion. *Adv. Funct. Mater.* **2024**, *34*, 2309426.

[13] Li, T.; Tsubaki, N.; Jin, Z. L. S-scheme heterojunction in photocatalytic hydrogen production. *J. Mater. Sci. Technol.* **2024**, *169*, 82–104.

[14] Song, W. T.; Chong, K. C.; Qi, G. B.; Xiao, Y. K.; Chen, G. W.; Li, B. W.; Tang, Y. F.; Zhang, X. Y.; Yao, Y. F.; Lin, Z. Q. et al. Unraveling the transformation from type-II to Z-scheme in perovskite-based heterostructures for enhanced photocatalytic CO_2 reduction. *J. Am. Chem. Soc.* **2024**, *146*, 3303–3314.

[15] Cui, W.; Yang, W. J.; Chen, P.; Chen, L.; Li, J. Y.; Sun, Y. J.; Zhou, Y.; Dong, F. Earth-abundant $CaCO_3$-based photocatalyst for enhanced ROS production, toxic by-product suppression, and efficient NO removal. *Energy Environ. Mater.* **2022**, *5*, 928–934.

[16] Jiang, C.; Qiu, Y. X.; Xin, X. X.; Li, Y. Y.; Li, H. L.; Wang, H.; Xu, J. X.; Lin, H. F.; Wang, L.; Turkevych, V. MOF-templated tubular $Ni_{1-x}Co_xS_2$–CdS heterojunction with intensified direct Z-scheme charge transmission for highly promoted visible-light photocatalysis. *Nano Res.* **2024**, *17*, 6281–6293.

[17] Zhou, Y. J.; Gao, K. J.; Song, Y. X.; Zhang, B. Y.; Dong, P. Y.; Xi, X. G.; Zhang, J. L. Binary direct vs. ternary electron-mediated Z-scheme heterojunctions: Unraveling pathway-engineered carrier dynamics for photocatalytic hydrogen evolution. *Appl. Catal. B: Environ. Energy* **2026**, *382*, 126002.

[18] Sharma, J.; Dhiman, P.; Kumar, A.; Sharma, G. Advances in photocatalytic NO oxidation by Z-scheme heterojunctions. *Environ. Res.* **2024**, *240*, 117431.

[19] Nie, C. L.; Wang, X. H.; Lu, P.; Zhu, Y. K.; Li, X.; Tang, H. Advancements in S-scheme heterojunction materials for photocatalytic environmental remediation. *J. Mater. Sci. Technol.* **2024**, *169*, 182–198.

[20] Zhong, X.; Zhu, Y. X.; Sun, Q. F.; Jiang, M.; Li, J. Q.; Yao, J. F. Tunable Z-scheme and Type II heterojunction of Cu_xO nanoparticles on carbon nitride nanotubes for enhanced visible-light ammonia synthesis. *Chem. Eng. J.* **2022**, *442*, 136156.

[21] Liang, X. X.; Zhao, J.; Wang, T.; Zhang, Z. X.; Qu, M.; Wang, C. Y. Constructing a Z-scheme heterojunction photocatalyst of $GaPO_4$/α-MoC/Ga_2O_3 without mingling type-II heterojunction for CO_2 reduction to CO. *ACS Appl. Mater. Interfaces* **2021**, *13*, 33034–33044.

[22] Gadore, V.; Mishra, S. R.; Ahmaruzzaman, M. Bandgap engineering approach for synthesising photoactive novel Ag/HAp/SnS_2 for removing toxic anti-fungal pharmaceutical from aqueous environment. *J. Hazard. Mater.* **2024**, *461*, 132458.

[23] Zhang, Y. J.; Zhou, K. L.; Yuan, C. Y.; Lv, H. J.; Yin, H. F.; Fei, Q.; Xiao, D. D.; Zhang, Y. Z.; Lau, W. *In-situ* formation of $SrTiO_3$/Ti_3C_2 MXene Schottky heterojunction for efficient photocatalytic hydrogen evolution. *J. Colloid Interface Sci.* **2024**, *653*, 482–492.

[24] Tenorio, M.; Moreno, C.; Febrer, P.; Castro-Esteban, J.; Ordejón, P.; Peña, D.; Pruneda, M.; Mugarza, A. Atomically sharp lateral superlattice heterojunctions built-in nitrogen-doped nanoporous graphene. *Adv. Mater.* **2022**, *34*, 2110099.

[25] Ye, L.; Yang, J. W.; Kim, D. P.; Sun, D. R. Advances in hydrophobic metal-organic frameworks (MOFs) for photo/electrocatalytic CO_2 reduction. *Nano Res.* **2026**, *19*, 94908041.

[26] Chu, X. Y.; Liu, S. K.; Luan, B. B.; Zhang, Y.; Xi, Y. M.; Shao, L. H.; Zhang, F. M.; Lan, Y. Q. Crystal-facet-controlled internal electric field in MOF/COF heterojunction towards efficient photocatalytic overall water splitting. *Angew. Chem., Int. Ed.* **2025**, *64*, e202422940.

[27] Wang, Y. N.; Jia, H. Y.; Lu, D. Y.; Wang, J. G.; Peng, T. Y. *In situ* fabrication of Cu^{II}-tetrapyridylporphyrin derived single-atom CuN_x cluster-modified TiO_2 for efficient hydrogen evolution reaction. *Nano Res.* **2025**, *18*, 94907499.

[28] Xu, M. S.; Zhu, P. F.; Cai, Q. H.; Bu, M. C.; Zhang, C. H.; Wu, H.; He, Y. Z.; Fu, M.; Li, S. Q.; Liu, X. Y. *In-situ* fabrication of TiO_2/NH_2-MIL-125(Ti) via MOF-driven strategy to promote efficient interfacial effects for enhancing photocatalytic NO removal activity. *Chin. Chem. Lett.* **2024**, *35*, 109524.

[29] Zhang, M.; Zhou, Y. L.; Zhang, H. W.; Yin, H. S.; Duan, J. R.; Ai, S. Y. Cu_2O-mediated heterojunction conversion from dual type II to dual Z-scheme: Its application in photoelectric-colorimetric dual-mode detection of fat mass and obesity-associated (FTO) protein. *Anal. Chem.* **2024**, *96*, 16080–16090.

[30] Yu, X.; Jin, X.; Chen, X. Y.; Wang, A. Z.; Zhang, J. M.; Zhang, J.; Zhao, Z. H.; Gao, M. M.; Razzari, L.; Liu, H. A microorganism bred TiO_2/Au/TiO_2 heterostructure for whispering gallery mode resonance assisted plasmonic photocatalysis. *ACS Nano* **2020**, *14*, 13876–13885.

[31] Wang, J.; Yao, J. M.; Yin, L. L.; Wang, B.; Liu, X.; Yuan, L.; Zhang, C. Q.; Bao, T.; Liu, C.; Hu, X. J. Facet engineering of metal-organic frameworks for efficient tetracycline degradation by photocatalytic activation of peroxymonosulfate. *Chem. Eng. J.* **2024**, *497*, 154836.

[32] Pancielejko, A.; Baluk, M. A.; Zagórska, H.; Miodyńska-Melzer, M.; Gołąbiewska, A.; Klimczuk, T.; Krawczyk, M.; Pawlyta, M.; Matus, K.; Mikolajczyk, A. et al. Cu-incorporated NH_2-MIL-125(Ti): A versatile visible-light-driven platform for enhanced photocatalytic H_2 generation and CO_2 photoconversion. *Mater. Horiz.* **2025**, *12*, 957–972.

[33] Liu, Y. Q.; Xin, X.; Shi, Y. H.; Zhao, Z. F.; Tan, J. D.; Yang, D.; Jiang, Z. Y. Three-ligand Ti-MOFs for high-efficient photocatalytic H_2 evolution. *Chem. Eng. J.* **2024**, *482*, 149193.

[34] Zhang, B. X.; Zhang, J. L.; Tan, X. N.; Shao, D.; Shi, J. B.; Zheng, L. R.; Zhang, J.; Yang, G. Y.; Han, B. X. MIL-125-NH_2@TiO_2 core–shell particles produced by a post-solvothermal route for high-performance photocatalytic H_2 production. *ACS Appl. Mater. Interfaces* **2018**, *10*, 16418–16423.

[35] Li, P.; Zhang, S.; Yang, X. Y.; Wang, X. Y.; Xie, Z. X.; He, H. M.; Sun, F. X.; Liu, J.; Li, J. Y. Integrating Au@MOF@COF nanocomposites for electrochemical aptasensing of trace oxytetracycline. *Nano Res.* **2025**, *18*, 94907590.

[36] Xu, Z. H.; Yue, W. H.; Li, C. C.; Wang, L. Z.; Xu, Y. K.; Ye, Z. W.; Zhang, J. L. Rational synthesis of Au-CdS composite photocatalysts for broad-spectrum photocatalytic hydrogen evolution. *ACS Nano* **2023**, *17*, 11655–11664.

[37] Xu, F. F.; Shang, D. Y.; Zhu, C. C.; Du, G. Z.; Shi, J. C.; Dong, X. F.;

Li, X. L.; Liang, X. M. *In situ* MXene-controlled synthesis of polycrystalline TiO_2 for highly efficient enrichment of phosphopeptides. *ACS Appl. Mater. Interfaces* **2025**, *17*, 260–268.

[38] Tu, B. Y.; Yu, K. F.; Fu, D. J.; Zhou, L.; Wang, R. X.; Jiang, X. Y.; Liu, H. H.; Cao, X.; Gong, X.; He, R. et al. Amino-rich Ag-NWs/NH_2-MIL-125(Ti) hybrid heterostructure via LSPR effect for photo-assist uranium extraction from fluorine-containing uranium wastewater without sacrificial agents. *Appl. Catal. B: Environ.* **2023**, *337*, 122965.

[39] Yoon, J. W.; Kim, J. H.; Jo, Y. M.; Lee, J. H. Heterojunction between bimetallic metal-organic framework and TiO_2: Band-structure engineering for effective photoelectrochemical water splitting. *Nano Res.* **2022**, *15*, 8502–8509.

[40] Liu, Y. Q.; Shi, Y. H.; Xin, X.; Zhao, Z. F.; Tan, J. D.; Yang, D.; Jiang, Z. Y. Boosting electron transfer of Ti-MOFs via electron-deficient boron doping for high-efficiency photocatalytic nitrogen fixation. *Appl. Catal. B: Environ. Energy* **2025**, *363*, 124815.

[41] Li, W. T.; Wu, N. N.; Li, C. Z.; Guo, J.; Zhang, G. X.; Pang, H. Facet engineering of NH_2-MIL-125(Ti) for enhanced synergistic adsorption and photocatalysis reduction of U(VI) under visible light. *Chin. Chem. Lett.* **2026**, *37*, 110733.

[42] He, Y. Z.; Li, H. F.; Wu, J.; Liu, Z. Y.; Chen, Y.; Guo, W. W.; Wu, Y. J.; Fu, M.; Liu, X. Y. *In-situ* formation of Au nanoparticles with surface plasmon resonance confined in the framework of Cu ions doped NH_2-MIL-125(Ti) to enhance photocatalytic hydrogen production and NO removal. *Appl. Surf. Sci.* **2022**, *604*, 154641.

[43] Zhang, B. F.; Zengcai, Z. Y.; Lin, W. T.; Zhang, M. J.; Pi, Y. H.; Wang, T. J. Confinement of Cu_2O by *in-situ* derived NH_2-MIL-125@TiO_2 for synergetic photothermal-driven hydrogen evolution from aqueous-phase methanol reforming. *Chem. Eng. J.* **2023**, *465*, 142904.

[44] Zhang, E. W.; Lu, H.; Zhang, W.; Cao, S. Y.; Wang, Y.; Rong, R.; Liu, Y.; Zhang, Z. H.; Yang, M.; Liu, Y. P. et al. Lifting surface reconstruction of Au(100) by tellurium adsorption. *Nano Res.* **2023**, *16*, 6967–6973.

[45] Li, Q. R.; Chang, H.; Gao, G. X.; Jian, H. R.; Liu, W. F.; Jia, H. S.; Xue, J. B.; Liu, H. R.; Shen, Q. Q. Cadmium doping induced type-II to Z-scheme switching in CdSe/$BiVO_4$ heterojunction for enhancing photocatalytic hydrogen production. *Sep. Purif. Technol.* **2025**, *353*, 128444.

[46] Wang, J.; Chen, C. C.; Zhao, Z. H.; Cheng, C.; Tang, Z. H.; Du, Z.; Wang, Y. F.; Pan, L. Construction of N-doped g-C_3N_4/NH_2-MIL-125(Ti) S-scheme heterojunction for enhanced photocatalytic degradation of organic pollutants: DFT calculation and mechanism study. *J. Alloys Compd.* **2022**, *922*, 166288.

[47] Xu, F. Y.; Meng, K.; Cheng, B.; Wang, S. Y.; Xu, J. S.; Yu, J. G. Unique S-scheme heterojunctions in self-assembled TiO_2/$CsPbBr_3$ hybrids for CO_2 photoreduction. *Nat. Commun.* **2020**, *11*, 4613.

[48] Zhang, R. Y.; Cao, Y. H.; Doronkin, D. E.; Ma, M. Z.; Dong, F.; Zhou, Y. Single-atom dispersed Zn–N_3 active sites bridging the interlayer of g-C_3N_4 to tune NO oxidation pathway for the inhibition of toxic by-product generation. *Chem. Eng. J.* **2023**, *454*, 140084.

[49] Zhang, W. D.; Ma, Y. R.; Song, C. X.; Wei, Y. P.; Chen, P.; Ai, W. X.; Wang, Y.; Dong, X.; Dong, F. Regulating adsorption activation of reactants by Bi–Cl synergistic sites for promoting photocatalytic NO deep oxidation. *Adv. Funct. Mater.* **2024**, *34*, 2410902.

[50] Shen, H. D.; Zhan, X. Y.; Hong, S.; Xu, L.; Yang, C. M.; Robertson, A. W.; Hao, L. D.; Fu, F.; Sun, Z. Y. Ultrafine MoO_x clusters anchored on g-C_3N_4 with nitrogen/oxygen dual defects for synergistic efficient O_2 activation and tetracycline photodegradation. *Nano Res.* **2023**, *16*, 10713–10723.

[51] Li, Y. H.; Zhang, M.; Chen, B. F.; Ouyang, P.; Duan, Y. Y.; Lv, K. L.; Dong, F. An ultrafast carrier dynamics system from oxygen vacancies modified SnO_2 QDs and Zn_2SnO_4 heterojunction for deeply photocatalytic oxidation of NO. *J. Mater. Sci. Technol.* **2023**, *165*, 85–93.

[52] Lei, B.; Cui, W.; Sheng, J. P.; Wang, H.; Chen, P.; Li, J. Y.; Sun, Y. J.; Dong, F. Synergistic effects of crystal structure and oxygen vacancy on Bi_2O_3 polymorphs: Intermediates activation, photocatalytic reaction efficiency, and conversion pathway. *Sci. Bull.* **2020**, *65*, 467–476.